



HAL
open science

Improving wavefront sensing with a Shack-Hartmann device

Martin Rais, Jean-Michel Morel, Carole Thiebaut, Jean-Marc Delvit, Gabriele Facciolo, Carole Thiebaud

► **To cite this version:**

Martin Rais, Jean-Michel Morel, Carole Thiebaut, Jean-Marc Delvit, Gabriele Facciolo, et al.. Improving wavefront sensing with a Shack-Hartmann device. Applied optics, 2016, 55 (28), 10.1364/AO.55.007836 . hal-01829646

HAL Id: hal-01829646

<https://enpc.hal.science/hal-01829646>

Submitted on 18 Jul 2018

HAL is a multi-disciplinary open access archive for the deposit and dissemination of scientific research documents, whether they are published or not. The documents may come from teaching and research institutions in France or abroad, or from public or private research centers.

L'archive ouverte pluridisciplinaire **HAL**, est destinée au dépôt et à la diffusion de documents scientifiques de niveau recherche, publiés ou non, émanant des établissements d'enseignement et de recherche français ou étrangers, des laboratoires publics ou privés.

Improving wavefront sensing with a Shack-Hartmann device

Martin Rais^{1,2,*}, Jean-Michel Morel², Carole Thiebaud³, Jean-Marc Delvit³, and Gabriele Facciolo^{2,4}

¹TAMI, Universitat des les Illes Balears, Carretera de Valdemosa km 7.5, Mallorca, Spain

²CMLA, ENS Cachan, Université Paris Saclay, 63 Avenue du President Wilson, 94235, Cachan CEDEX, France

³CNES, Toulouse, France

⁴LIGM (UMR CNRS 8049), ENPC, Université Paris-Est, France

*Corresponding author: martin.rais@cmla.ens-cachan.fr

Compiled: June 16, 2016

Abstract

In order to achieve higher resolutions, current earth-observation satellites use larger lightweight primary mirrors that can deform over time, impacting on image quality. We evaluated the possibility of compensating these deformations directly in the satellite by combining a deformable mirror with a Shack-Hartman wavefront sensor (SHWFS). The performance of the SHWFS depends entirely on the accuracy of the shift estimation algorithm employed, which should be computationally cheap to be executed on-board. We analyzed the problem of fast accurate shift estimation in this context and propose a new algorithm, based on a global optical flow method that estimates the shifts in linear time. In our experiments, our method proved to be more accurate and stable, as well as less sensitive to noise than all current state-of-the-art methods, permitting a more precise on-board wavefront estimation.

1 Introduction

Adaptive optics (AO) is a well-known technology to sense and correct wavefront distortions. This technology is used in astronomy to produce sharper images from heavily aberrated wavefronts originated by atmospheric turbulence. This correction is usually performed through a deformable mirror which adapts to the measured wavefront correcting the distortion [48]. Since AO also allows to improve the performance of aberrated optical systems, it is widely used in several other contexts such as ophthalmology [47], microscopy [6] and free-space laser communication systems [45] among others [44].

A key component of an adaptive optics system is the wavefront sensing mechanism, i.e., the device used to precisely measure the distortion. A Shack-Hartmann wavefront sensor (SHWFS) is one such device. It uses an array of lenslets to measure the deformation of the incoming wavefront. The shift of each lenslet focal plane image is proportional to the mean slope of the wavefront in the subaperture onto this lenslet. It yields a discrete local approximation of the slope of the wavefront (Fig. 1). This deformation is usually measured by imaging a point source such as a star, and measuring the relative displacement between a reference image and all other subimages to compute the local gradient of the wavefront.

Recently, the community evaluated the possibility of cor-

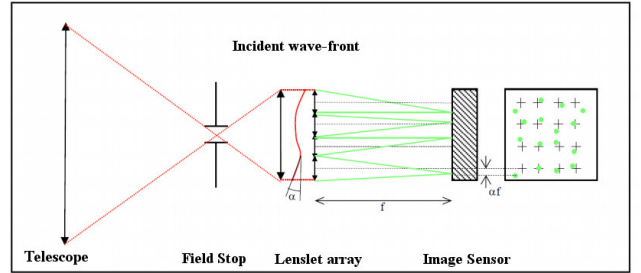


Figure 1: A Shack-Hartmann Wavefront Sensor measures the wavefront by computing the local shifts between the detected spots (in green) and the reference crosses (in black), which would occur if no deformation were present.

recting wavefront deformations on earth-observation satellites [26, 11, 5] caused by the deformation of the primary mirror. In this setting, the problem of atmospheric turbulence is negligible. Indeed, in astronomical observations from the earth, the angle of view is extremely narrow. As a result, the light wavefront crosses a narrow solid angle of atmosphere and its perturbations due to turbulence have a great impact on image quality. In earth observation from a satellite, however, the angle of view is much larger, so the perturbations due to turbulence are relatively much smaller.

However, the correction of optical aberration is becoming more and more important for high resolution earth-observation satellites. Indeed, in order to increase the spatial resolution of satellite images, i.e., its ground sample distance, a larger primary mirror is required to gain a higher angular resolution. Large mirrors must be thicker to avoid deformations which increases dramatically their weight and renders launching costs prohibitive. For this reason large yet lighter mirrors have to be considered. Their drawback is that time-varying deformations due to thermal effects and vibration severely deteriorate the image quality [8]. To correct these deformations, a SHWFS device could be used to measure them by observing the earth, together with a deformable mirror to compensate for these deformations. As opposed to adaptive optics where the distortion has to be compensated in real-time due to the fast changes in the atmosphere, in our case the compensation for the mirror deformation is less frequent, roughly on timescales of seconds.

Coming from control theory, two schemes exist for performing wavefront correction. While in an *open loop* adaptive

optics system the wavefront error is measured before it has been corrected by the wavefront corrector, in a *closed loop* system the measured wavefront deformation is the residual error after the correction of the previous estimation has been performed. The difference between both operational modes is important because in a *closed loop* system, the wavefront aberrations measured will be small, permitting to assume a maximum shift between images of up to a few pixels. In this article we assume a *closed loop* system.

Another important factor that affects the accuracy of wavefront sensing is the phenomenon of scintillation and phase anisoplanatism, which results in more complex patterns than simple global shifts between subapertures. The influence of this phenomenon was widely studied in the context of adaptive optics [28, 30, 46]. However, in remote sensing, because the phase aberration is produced at the telescope pupil, all parts of the image are affected by it in the same way, neglecting its incidence [28].

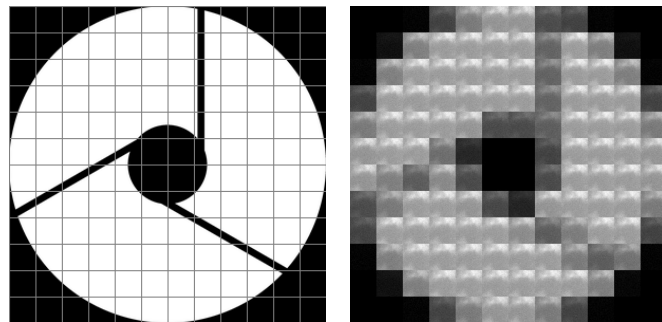
Finally, once the shift estimation is performed, several methods can be used to reconstruct the wavefront from its local gradient estimations, namely the iterative zonal method [41], the vector-matrix-multiply (VMM) method [15] and the Fourier Transform Reconstruction (FTR) method [27]. The latter is recommended when the number of actuators is high, however, the VMM method obtains more accurate results under a SHWFS configuration using less than 12×12 subapertures [33].

As mentioned before, wavefront sensing in astronomy is usually performed using the stars. When observing the earth from space this task becomes more challenging.

Extended scene vs point source observation. For an earth observation satellite, the SHWFS is used on extended scenes instead of point sources such as stars. This setup is called scene-based wave-front sensing (SBWFS), or extended-scene wave-front sensing (ESWFS). Because the scene is extended, a field stop has to be installed in front of the SHWFS, as seen in Fig. 1, so that the images given by the lenslet array do not overlap in the lenslet focal plane [20]. This yields a grid of images, each one corresponding to one sub-aperture, which are shifted versions of the same scene. Accurately measuring these shifts permits to estimate the gradient of the wavefront. As a drawback, since we are dealing with landscapes larger than the captured image, achieving high accuracy on the shift estimation task gets challenging. Worse still, in most wavefront sensors, the extent of the source object normally reduces the contrast of the signal, thwarting accurate shift measurements [35].

Difference in subimage SNRs due to pupil occlusions. For long focal length telescopes commonly used on earth-observation satellites, the Korsch concept is the most common. The pupil of a Korsch telescope is generally occluded in the center by a secondary mirror. The arms used to hold this mirror also occlude the pupil. In these regions, the lenslets suffer a loss in the incoming signal, proportional to their percentage of occlusion. This configuration is depicted in Fig. 2a. An example of a SHWFS output in the CRT sensor is shown in Fig. 2b. From this figure, it can be seen how the SNR on the partially occluded lenslets is significantly lower.

Limited on-board computational capacity. An important distinction when performing wavefront sensing from earth-observation satellites is its limited computational ca-



(a) Occlusion schema in a 12×12 SHWFS. (b) Images obtained on an extended landscape.

Figure 2: Example of a SHWFS occlusion scheme under a Korsch telescope. Both the secondary mirror and the arms used to hold it are clearly visible. For each lenslet, the decrease of the incoming signal is proportional to its occlusion.

capacity. Due to this constraint, several shift estimation methods proposed for SHWFS are not suitable on-board due to their high complexity.

Unusable observations. Another difference when observing extended scenes, as opposed to the use of SHWFS with point sources, is the need to predict if the current scene permits to accurately estimate the wavefront aberration. Scenes such as clouds, sea or any textureless landscape can thwart all shift measurement methods, leading to poor wavefront estimation.

Contributions. Based on these differences, we present a new shift estimation method in the context of SHWFS used on extended scenes. Our contribution is threefold. We shall start with a review of the state-of-the-art on wavefront correction using SHWFS on extended scenes. Second, we propose the use of an iterative global optical flow method for shift estimation which presents several advantages over the conventional correlation methods. Third, we propose a fast and effective method for scene preselection that adds almost no further computational cost to the overall estimation using the proposed algorithm.

This article is organized as follows. In section 2 we review the state-of-the-art on shift estimation applied for SHWFS on extended scenes. In section 3 we present our optical flow method and its usage for wavefront correction from earth-observation satellites. In section 4 we focus on scene preselection methods. In section 5 we study the influence of the parameters on the proposed method, and thoroughly compare its performance with the state-of-the-art. We involve ground truth simulations provided by CNES and our own simulator. Section 6 is a conclusion.

2 State-of-the-art review

Since the Shack-Hartmann wavefront sensor was introduced in the late 1960s [25], several algorithms were proposed to estimate the shifts using point sources such as stars. However, only few authors have studied the problem when the source is extended, as when observing the earth from space. Broadly, they can be categorized in correlation methods working in the spatial [21, 20, 18] or in the frequency domain

[26, 37, 39, 17, 18], phase correlation methods that estimate the shift directly in the frequency domain [17, 42], iterative methods [37, 39] that improve on previous approaches by progressively estimating the shift, and maximum likelihood (ML) approaches [14] that incorporate a specific noise model to the problem and compute ML estimate as the solution of an optimization problem.

2.1 Correlation-based Methods

These methods compute a correlation score on a grid $C(i, j)$ and interpolate it to determine the subpixel location of the peak. The methods mainly differ in the choices of correlation score and interpolation strategy.

Spatial domain correlation-based methods. Michau *et al.* [21] were among the first to propose an experimental implementation for using a SHWFS on extended sources larger than the wavefront sensor field of view. Their method computes the discrete cross-correlation between the images and a reference subimage chosen from the central region of the wavefront sensor image pattern. To estimate the subpixel shifts, the correlation peak location is computed as the centroid of the pixels with a correlation higher than half the maximal observed correlation.

Löfdahl [18] tested several shift estimation algorithms for Shack-Hartmann wavefront sensors observing the sun. By testing with several possible sources of errors such as noise, blur and bias mismatch, he evaluated five different correlation-based methods to obtain the correlation score $C(i, j)$. Among the evaluated correlation algorithms, the best all-around performer proved to be the classical least squares approach or squared difference function (SDF). Another proposed correlation score is the Covariance Function in the Image domain (CFI) using trend-corrected versions of both images. Indeed, Smithson & Tarbell [43] showed that a linear trend in intensity shifts the covariance peak from the correct position, so a fitted plane has to be subtracted from both images beforehand. For the SHWFS case, this reduces to simply subtracting the mean value for each image. They also tested other two methods based on the absolute difference between both images (ADF), and its square (ADF²) in order to better locate the minimum at the sub-pixel level.

To achieve subpixel precision, they evaluated four interpolation strategies to look for the minimum value on the correlation grid $C(i_{min}, j_{min})$. The four algorithms they evaluated can be described as fitting a conic section to the 3×3 -element submatrix s centered in the sample minimum $C(i_{min}, j_{min})$. The evaluated algorithms differ on the number of pixels used and on whether the fitting is done in 2D or in each dimension separately. The 1D quadratic interpolation (1QI) fits a parabola in each dimension independently, while the 2D quadratic interpolation (2QI) fits the conic to the 3×3 neighborhood. They also evaluated a 1D Least Square (1LS) method on both dimensions, which averages the three values on one dimension and then applies least squares on the other, and a 2D Least Square (2LS) variant which includes the corner values in the procedure.

Frequency domain correlation-based methods. Poyneer [26] studied the wavefront estimation problem

using a SHWFS by observing the Earth from space using lightweight optics. By assuming periodicity on the input images, the author points out that minimizing the MSE between both images becomes equivalent to maximizing their periodic convolution, which is efficiently computed in the frequency domain using the cross-correlation theorem. To get subpixel precision the maximum at integer coordinates is refined by independently fitting a parabola on each dimension.

Löfdahl also evaluated a frequency-domain method [18] which, similarly to [26], computes the covariance in the Fourier domain (CFF). However, both images are previously normalized to zero mean and windowed with a 2D Hamming window or a flat-top window to avoid ringing caused by the periodization. Again, the subpixel maximum is obtained by fitting a parabola to the grid.

2.2 Phase Correlation

The phase-correlation method was widely studied in the image processing domain [42, 12]. Let $I(i, j)$ be an $M \times N$ image, due to the Fourier shift theorem we know that

$$\mathcal{F}\{I(i-\Delta_x, j-\Delta_y)\} = \hat{I}(u, v) \exp\left(-j2\pi\left(\frac{u\Delta_x}{M} + \frac{v\Delta_y}{N}\right)\right) \quad (1)$$

then by computing the cross-power spectrum between both images and extracting the phase for each frequency, the matrix ϕ , called the phase correlation matrix, is given by

$$\arg(\hat{C})(u, v) = \phi(u, v) = 2\pi\left(\frac{u\Delta_x}{M} + \frac{v\Delta_y}{N}\right). \quad (2)$$

The shifts can therefore be computed directly in the frequency domain by fitting a plane passing through the origin of $\phi(u, v)$. Due to aliasing, some of these frequencies may be corrupted and distort the shift estimation. To avoid this problem Knutsson *et al.* [17] discard most of the corrupted frequencies from ϕ retaining only the two or four lowest frequencies. This estimate has the advantage of being the least sensitive to aliasing [42] hence the most reliable. Moreover assuming small shifts (smaller than half pixel) no phase unwrapping is required [13]. The accuracy of these methods however, suffers considerably in low SNR situations [26].

2.3 Iterated Estimation

Since correlation-based shift estimation has a bias proportional to the shift magnitude [23], then compensating the shift by resampling one of the images and iterating should progressively reduce this bias (see section 3).

Sidick *et al.* [37] proposed Adaptive Cross-Correlation (ACC) that estimates the shift using an approach similar to Knutsson [17] and uses this estimation to resample the second image in the frequency domain to iterate the procedure. Due to potential ringing artifacts on the image boundaries after the resampling procedure, the shift is estimated using the central part of both images with size $N/2$, involving one fourth of the image pixels in the computation. To make the shift estimation more accurate, it uses eight frequency components $\phi(n, m)$ with $0 \leq m, n \leq 2$ to perform

the least-squares fitting, excluding the center. This procedure is made iterative by accumulating both u and v shift estimates, until a predefined amount of iterations is reached or until $\Delta_s = [\Delta_x^2 + \Delta_y^2]^{1/2}$, the increase of both shift estimates, is lower than a predefined tolerance value. This technique is then applied for every sub-aperture $I_k(i, j)$.

This algorithm was evaluated on simulated scenes by varying the shift between them [37] and by using a real SHWFS configuration testbed [38] produced in the Jet Propulsion Laboratory at NASA [22]. By relaxing the tolerance parameter of their iterative scheme, it achieves errors of the order of 0.05 pixels by using between 3 and 6 iterations.

This method presents two problems. Since it discards half of each image to perform the shift estimation, it usually fails when image contents appear away from the center. Also, as in [17], the shift estimation step of the method suffers severely in low SNR scenarios. Due to this reason, the authors updated the method in [39] by replacing this step with the periodic-correlation technique of Poyneer [26]. This method, named Adaptive Periodic Correlation (APC), is more tolerant to noise than ACC.

2.4 Maximum Likelihood Estimator

Gratadour et al. [14] studied the performance of the MLE within an adaptive optics context. Assuming that the two images I_0 and I_1 are unknown and contaminated with Gaussian noise their method reduces to minimizing

$$\sum_k (4\sigma^2(k))^{-1} |I_1(k) - [I_0(x - x_1)]_{III}(k)|^2, \quad (3)$$

with respect to the shift x_1 , where $\sigma^2(k)$ is the noise variance at pixel k and $[\]_{III}$ a sampling operator that performs Fourier resampling, which is done by computing the inverse FFT of (1). To guarantee that the images can be resampled in the Fourier domain they are pre-filtered using a low-pass filter. This minimization is performed using an a conjugate gradient method. Although it improves over the typical cross-correlation, it has high computational cost prohibiting its implementation on satellites [20, 26].

3 Accurate shift estimation using optical flow in the context of a SHWFS

In order to estimate the shift between two sub-apertures, we propose to use a gradient-based shift estimator (GBSE) based on the optical flow equation. The idea behind this methodology, as proposed originally by Lucas and Kanade [19], is to relate the difference between two successive frames to the spatial intensity gradient of the first image. Given the two images $I_2(x, y) = I_1(x - v_x, y - v_y)$ where v_x and v_y are the unknown shift coefficients, the first order Taylor approximation yields

$$I_1(x, y) - I_2(x, y) \approx v_x \frac{\partial I_1(x, y)}{\partial x} + v_y \frac{\partial I_1(x, y)}{\partial y}. \quad (4)$$

To estimate the global optical flow between I_1 and I_2 , the Lucas-Kanade algorithm assumes a constant flow for every

pixel, which allows the construction of an overdetermined system of constraint equations $\mathbf{A}\mathbf{v} = \mathbf{b}$, where \mathbf{A} is composed of spatial intensity derivatives and \mathbf{b} has temporal derivatives. Emulating Simoncelli [40], in order to increase the accuracy of the method by minimizing noise or aliasing influence, we looked for two kernel functions: an anti-symmetric kernel \mathbf{d} to estimate the image gradients and a symmetric kernel \mathbf{k} to prefilter the images. Using both kernels, matrix \mathbf{A} and vector \mathbf{b} become

$$\mathbf{A} = \begin{pmatrix} (\mathbf{d}_x * I_1)(p_1) & (\mathbf{d}_y * I_1)(p_1) \\ \vdots & \vdots \\ (\mathbf{d}_x * I_1)(p_n) & (\mathbf{d}_y * I_1)(p_n) \end{pmatrix}, \mathbf{b} = \begin{pmatrix} (\mathbf{k} * (I_1 - I_2))(p_1) \\ \vdots \\ (\mathbf{k} * (I_1 - I_2))(p_n) \end{pmatrix} \quad (5)$$

where p_i with $i = 1 \dots n$ represents the i th pixel and n the image size. The shift is obtained by Moore-Penrose pseudo-inversion

$$\begin{bmatrix} v_x \\ v_y \end{bmatrix} = \underbrace{\begin{bmatrix} \sum I_x^2 & \sum I_x I_y \\ \sum I_x I_y & \sum I_y^2 \end{bmatrix}}_{\mathbf{A}^T \mathbf{A}}^{-1} \underbrace{\begin{bmatrix} \sum I_t I_x \\ \sum I_t I_y \end{bmatrix}}_{\mathbf{A}^T \mathbf{b}} \quad (6)$$

where I_x, I_y stands for $\mathbf{d}_x * I_1$ and $\mathbf{d}_y * I_1$ respectively, and $I_t = \mathbf{k} * (I_1 - I_2)$ is the derivative over time.

It is no coincidence that the results of the method depend on the inversion of this second moment matrix. As will be shown later, the determinant of this matrix is crucial for determining the limits on the estimation performance. This matrix will be used to discard ill-posed cases before actually performing the shift estimation. The classic rejection case is when the gradient is mostly oriented in a single direction. This unsolvable situation is known as the aperture problem. Its detection by using the Cramer-Rao lower bounds is detailed in section 4.

It is important to remark that by centering the Taylor development at 0 and taking up to the first order term, the method gets systematically biased and becomes less precise as the shift gets higher, i.e., estimated shifts larger than one pixel would not be correctly estimated. Furthermore, the noise in the input images is completely ignored by the algorithm, which also impacts on its performance. Both these bias sources are studied in detail in [31, 23] and will be addressed next.

3.1 Iterative gradient-based shift estimator

Instead of dealing with the bias explicitly, it was shown in Pham et al. [23] that both bias sources depend linearly on the shift magnitude. This justifies the use of an iterative method, which is able to significantly reduce the bias, provided an appropriate resampling method is used. Algorithm 1 performs k iterations, computing the shift $v[i]$ by solving (6) (*findshift*), and iterates by reinterpolating the original image I_2 (*Resample*) using the total accumulated shift w . It is a variant of the Lucas-Kanade algorithm [19] known as Inverse Compositional Algorithm [3], in which the gradients of the reference image are static throughout the iterations, so $(\mathbf{A}^T \mathbf{A})^{-1}$ is only computed once.

In the next sections we will see that the gradient discretization used by *findshift* and the choice of interpolation method for image resampling are crucial for the precision of the GBSE method.

Algorithm 1 Iterative GBSE method.

```

1: procedure ILK( $I_1, I_2$ )      ▷ Receives a pair of images
2:    $i \leftarrow 0$ ;  $I_2[0] \leftarrow I_2$ ;  $w \leftarrow 0$ ;
3:   while  $i \leq k$  do
4:      $v[i] \leftarrow \text{findshift}(I_1, I_2[i])$       ▷ (6)
5:      $w \leftarrow w + v[i]$       ▷ Accumulate total shift
6:      $I_2[i+1] \leftarrow \text{Resample}(I_2, -w)$     ▷ Use the original
        $I_2$ 
7:      $i \leftarrow i + 1$ 
8:   return  $w$       ▷ Return accumulated shift

```

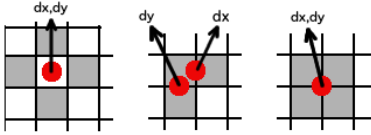


Figure 3: Used pixels (gray background) for fast gradient estimation methods and their exact localization (red dots). **Left:** Centered differences. **Center:** 1D backward difference for both ∂x and ∂y . **Right:** 2D backward difference.

3.2 Gradient computation and image pre-filtering

Gradient computation for optical flow methods has been thoroughly studied [40, 10, 32]. Since our shift estimation is focused on accuracy and the image size on SHWFS is typically small (usually smaller than 50×50 pixels), using a large kernel for computing image derivatives implies losing valuable boundary values. This constrains the kernel to be compact yet precise and robust to noise. In fact, the impact on the accuracy and the robustness to noise of the gradient computation is a key factor to the final performance of the GBSE method.

Because the method should be computationally fast, only simple schemes could be afforded. A straightforward candidate is the centered differences kernel $[1, 0, -1]$, however since the central pixel is ignored in the computation, its precision could be improved by taking contiguous pixels. For this reason, a backward difference kernel $[1, -1]$ would seem more appropriate. However, the corresponding center of this derivative differs for each component as seen from the middle image of Fig. 3.

A more precise gradient estimation method, illustrated on the right of Fig. 3, computes the derivatives by performing convolution with \mathbf{d}_x and \mathbf{d}_y given by

$$\mathbf{d}_x = \begin{bmatrix} 1/2 & -1/2 \\ 1/2 & -1/2 \end{bmatrix} \quad \mathbf{d}_y = \begin{bmatrix} 1/2 & 1/2 \\ -1/2 & -1/2 \end{bmatrix}, \quad (7)$$

and computes the vector \mathbf{b} in (5) by prefiltering both I_1 and I_2 using the half pixel bilinear shift kernel

$$\mathbf{k} = \begin{bmatrix} 1/4 & 1/4 \\ 1/4 & 1/4 \end{bmatrix}. \quad (8)$$

This gradient estimation procedure called *hypomode* [34], despite being simplistic usually improves the accuracy obtained by GBSE methods using finite difference gradient estimation. This is because it slightly blurs the input images, which alleviates both aliasing and noise.

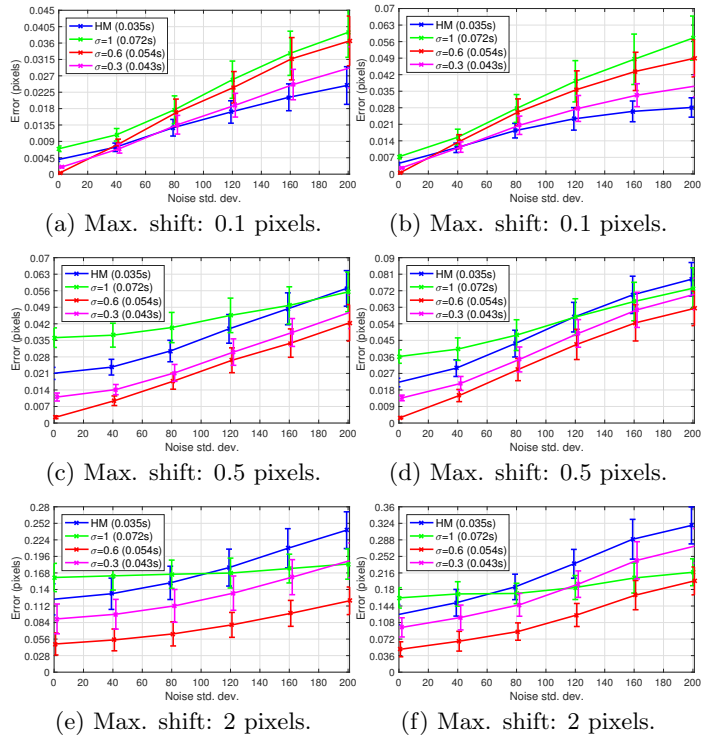


Figure 4: Gradient estimation methods comparison for three different maximum shifts (0.1, 0.5 and 2 pixels). **Left:** Highly contrasted image (simple case). **Right:** Gradients mainly distributed on a single direction (challenging case). Noise std. dev. according to 12-bit images.

We also considered the normalized 2D Gaussian smoothing kernel $\mathbf{k} = g(x, y, \sigma_g)$ with standard deviation σ_g , and its derivatives $\mathbf{d}_x = -\frac{x}{\sigma_g^2} g(x, y, \sigma_g)$ and $\mathbf{d}_y = -\frac{y}{\sigma_g^2} g(x, y, \sigma_g)$. The parameter σ_g controls the amount of blur, thus using a small value would be less tolerant to noise, while a high value could remove textures useful for the shift estimation. In our experiments, we evaluated using $\sigma_g = \{0.3, 0.6, 1\}$ with supports of 3, 5 and 7 pixels respectively.

As seen from both Fig. 4a and Fig. 4b, the fastest and most accurate gradient estimator for small shifts (≈ 0.1) is the *hypomode*. Therefore it should be considered when the underlying deformations are small enough (which could happen on a closed loop system with frequent mirror corrections). However, if the maximum shift caused by the wavefront aberration is larger than half a pixel, computing the Gaussian derivatives with $\sigma_g = 0.6$ offers the best balance between accuracy and tolerance against noise, as seen from figures 4c, 4d, 4e and 4f. In fact, using $\sigma = 0.6$ gives better results than using $\sigma = 0.3$. This is because a higher σ removes more noise from the derivatives, and blurring the images impacts less on the accuracy than neglecting the noise. Finally, it should be noted that although taking $\sigma = 1$ usually offers poor accuracy with small image sizes, its tolerance to noise becomes a decisive factor as the noise increases (as seen in figures 4e and 4f).

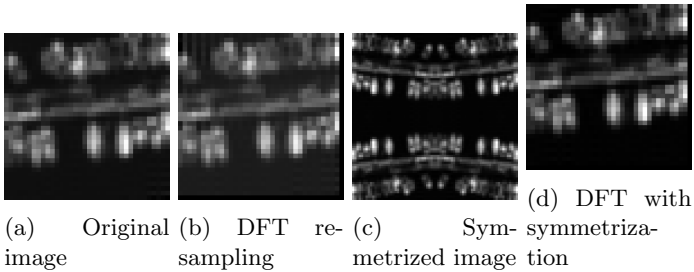


Figure 5: Example of FFT resampling with and without image symmetrization. Resampling with DFT produces ringing due to the discontinuities at the periodized boundaries. No visible ringing is observed after resampling with symmetrization.

3.3 Interpolation methods for image resampling

In order to iterate the method, the second image needs to be shifted, as indicated in step 6 of Algorithm 1. To this end, five different interpolation methods were evaluated, namely bilinear, bicubic [16] and cubic spline [9], together with resampling using the Fourier shift theorem [4], which is evaluated with and without image periodization. Image periodization prevents the generation of ringing artifacts due to the discontinuities at the image boundaries. It amounts to resampling with DFT a mirrored version of the image which has no discontinuities when periodization is assumed (see Fig.5).

The choice of interpolation method is critical for the overall method accuracy. However precision comes at a higher processing cost. We evaluated the different interpolations by simulating a landscape with noise of $\sigma_n = 80$, displacements between subapertures of up to 2 pixels, and computing gradients by using Gaussian derivatives with $\sigma_g = 0.6$. For each method we computed the average error and standard deviation over 200 independent random realizations, using the GBSE method with 2 and 3 iterations. Results in Fig. 6 show a non-negligible performance difference between the methods. In terms of average error, both DFT-based methods achieve the best results, however no significant improvement is obtained by performing periodization, although a minimal reduction in the standard deviation is observed. The splines interpolation yields slightly less accurate results, however it should be considered if fast DFT hardware cannot be installed on board. Finally, both bicubic and bilinear interpolation perform significantly worse than the rest, although bicubic interpolation results had less variability with respect to other approaches. Lastly using three iterations does not improve considerably over using two, not justifying the increase in computational cost. However, although not shown in this experiment, this difference gets higher as the noise increases, which justifies its use.

3.4 Image intensities equalization

One requirement of the GBSE algorithm is to work on images with similar intensities. Since occluded sub-apertures receive less light, their intensities differ from the reference image. To this end, all subimages are equalized by normalizing their mean with the highest mean among all subapertures.

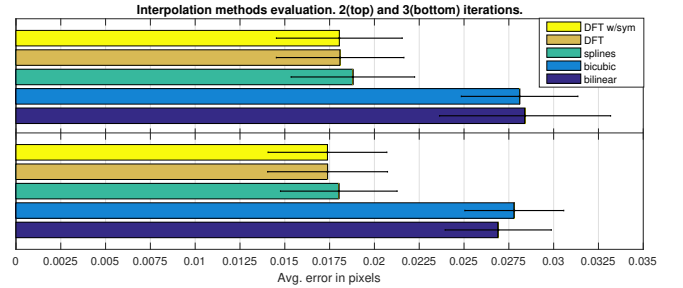


Figure 6: Comparison of evaluated interpolation methods using 2 and 3 iterations and Gaussian derivatives with $\sigma_g = 0.6$. Image noise was fixed to $\sigma_n = 80$ and the maximum displacement was set to 2 pixels.

When the point spread function (PSF) of each sub-aperture is known, another equalization strategy before shift estimation between a subaperture and the reference is to convolve both images with the PSF of the other one [5]. Our focus being on the shift estimation method, we chose to perform the equalization by the simple procedure explained above. It is computationally cheaper, yet obtains excellent results.

3.5 Multiscale implementation

The GBSE algorithm can be easily adapted to work in an open loop environment where aberrations are potentially larger, leading to larger shifts between subapertures. As mentioned before, if the shift is larger than one pixel, the GBSE method fails. However, by building a pyramid representation of the input images, (6) can be applied on each scale to estimate the shift between images, and this estimated shift can in turn be used to resample the second image on the following level of the pyramid. If more accuracy is desired, Algorithm 1 can be used to better estimate the shift at each scale. We compute the pyramid using an approximate dyadic Gaussian pyramid [7]. Starting from the coarse image at scale $n > 1$, the method is summarized in Algorithm 2.

Algorithm 2 Multiscale GBSE method.

```

1: procedure MSSE( $I_1, I_2$ )  ▷ Receives a pair of images
2:    $I_1^{1\dots n} \leftarrow \text{BuildPyramid}(I_1, n)$   ▷ Burt&Adelson's Gaussian Pyramid [7]
3:    $I_2^{1\dots n} \leftarrow \text{BuildPyramid}(I_2, n)$   ▷ i.e., IMPYRAMID function from Matlab
4:    $i \leftarrow n$ ;  $w \leftarrow 0$   ▷  $n$ : number of scales,  $w$ : accumulated shift
5:   while  $i > 1$  do
6:      $v(i) \leftarrow \text{ILK}(I_1^i, I_2^i)$  or  $\text{findshift}(I_1^i, I_2^i)$   ▷ Alg. 1 or (6)
7:      $w \leftarrow 2w + 2v(i)$ 
8:      $I_2^{i-1} \leftarrow \text{Resample}(I_2^{i-1}, -w)$ 
9:      $i \leftarrow i - 1$ 
10:   $v(1) = \text{findshift}(I_1^1, I_2^1)$ 
11:  return  $w + v(1)$   ▷ Return accumulated shift

```

4 Scene preselection and robustness estimation

Before evaluating the deformation of the incoming wavefront, it is crucial to determine if the current landscape, i.e., what the satellite is observing at the moment, is suitable for performing wavefront sensing. This problem has been studied by Sidick *et al.* [38] and by Poyneer [26] who proposed several fail-safe criteria to determine if a SH image is acceptable.

In this context, we propose to perform two distinct validations to ensure an accurate wavefront correction. While the first one is based on calculating the lowest theoretical achievable error through the Cramer-Rao lower bound (CRLB) given by the noise and the image contents, the second validation, called the eigenratio test, measures the gradient distribution along the image through the ratio of the eigenvalues of the structure tensor. Both validations are complementary and should be verified together.

CRLB test The best achievable accuracy, given the current landscape and the underlying noise, can be estimated by the Cramer-Rao lower bound. In the last decade, three main works have addressed the calculation of the error on the estimated shift caused by the noise. Robinson and Milanfar [31] used the Cramer-Rao lower bound to derive a performance limit for image registration. The CRLB imposes a lower limit on the mean squared error for any estimate of a deterministic parameter. Pham *et al.* [23] continued on the same idea to derive a theoretical limit for image registration, followed by a study of the bias for the gradient based 2D shift estimation. Recently, Aguerrebere *et al.* [1] performed an in depth study of performance limits within a multi-image alignment context and derived several Cramer-Rao lower bounds depending on the conditioning of the problem.

By assuming that the noise is independent, homoscedastic, Gaussian and with the same variance σ_n^2 on both images, and denoting by S the set of all pixels in the image, the Cramer-Rao bound for any unbiased 2D shift estimator is

$$\text{var}(v_x) \geq \frac{\sigma_n^2 \sum_S I_y^2}{\text{Det}} \quad \text{var}(v_y) \geq \frac{\sigma_n^2 \sum_S I_x^2}{\text{Det}} \quad (9)$$

where $\text{Det} = \sum_S I_x^2 \sum_S I_y^2 - (\sum_S I_x I_y)^2$. We can therefore define a parameter Δ_{CRLB} , the maximum allowed error in pixels, that determines whether the current landscape is acceptable for performing wavefront estimation, by verifying

$$(\text{var}(v_x) + \text{var}(v_y))^{1/2} \leq \Delta_{\text{CRLB}}. \quad (10)$$

Yet, I_x, I_y represent the gradient obtained from the unknown noiseless image I . Thus this bound is only useful for a theoretical study. In practice, however, the required values can be approximated using the method of [24], where they estimate the second moment matrix of image I_1 from noisy versions \tilde{I}_1 and \tilde{I}_2 . Another possibility would be to approximate these sums by computing the expected value using the derivative definition and a noise variance estimation. For example set $I_x(i, j) = I(i+1, j) - I(i, j)$ and let $\tilde{I} = I + n$ be the observed noisy image where n has distribution $\mathcal{N}(0, \sigma_n^2)$. Since all $n(i, j)$ are independent, by the law of large numbers

we have

$$\sum_S \tilde{I}_x^2 = \sum_S (I_x + n_x)^2 = \sum_S I_x^2 + \sum_S I_x n_x + \sum_S n_x^2 \simeq \sum_S I_x^2 + 2|S|\sigma_n^2.$$

It follows that we can estimate $\sum_S I_x^2$ from the noisy image \tilde{I} by

$$\sum_S I_x^2 \simeq \sum_S \tilde{I}_x^2 - 2|S|\sigma_n^2. \quad (11)$$

The other terms can be computed using similar calculations.

The CRLB defined in (9) expresses a direct relationship between the accuracy of the estimation and the SNR ratio, measured as a ratio of the noise to the square of the gradient. Furthermore, it follows from the form of the denominator of these expressions that if there is a strong correlation between I_x and I_y , the vertical and horizontal partial derivatives, then Det will be zero or very close to zero. The formulas show that this entails a high variance for the estimation of the translation. This is the so called Aperture Problem [36]. In that case the true motion is irrecoverable.

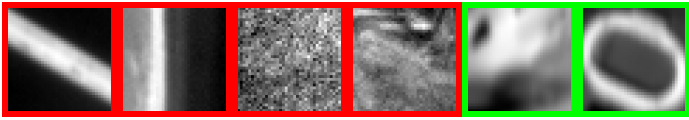
It must be noted that the Cramer-Rao bounds are derived for an unbiased 2D shift estimation. For the case of biased estimators, the bound is even higher. Also, the hypothesis made about the noise being white Gaussian and homoscedastic does not hold in a SHWFS context used from earth-observation satellites. However, the noise model for the sensor is usually known beforehand, therefore allowing its variance to be stabilized by applying a variance stabilization transform (VST) such as the well-known Anscombe transform [2].

Finally, for the case of SHWFS, since shifts between images are independent, the limit on the registration accuracy is imposed by estimating the shift between two frames.

Eigenratio test As noted by [1], the CRLB is less precise where it is most needed, namely when the signal is dominated by noise. Indeed, in that case the numerator and denominator of (9) cannot be estimated reliably, being both the difference of equivalent terms. This is why we will be forced to recur to more robust safety computations.

We propose to rapidly discard a landscape for a shift estimation by involving the eigenratio score of the second moment matrix $\tau = \mathbf{A}^T \mathbf{A}$ of (6). The matrix τ is also the structure tensor with unit weights associated to the image I_1 . The eigenvalues λ_1, λ_2 of τ and their corresponding eigenvectors e_1, e_2 summarize the distribution of the image gradient $\nabla I = (I_x, I_y)$. Namely, if $\lambda_1 > \lambda_2$, then e_1 (or $-e_1$) is the direction that is maximally aligned with the gradient within the image. More generally, the value of λ_k , for $k \in \{1, 2\}$, is the average of the square of the directional derivative of I along e_k . The relative discrepancy between the two eigenvalues is an indicator of the degree of anisotropy of the gradient in the image, measuring how strongly it is biased towards a particular direction (and its opposite). Then by calculating the ratio λ_2/λ_1 , we obtain a number between 0 and 1, characterizing the dominance of a particular direction for the gradients of the image. Empirically it was verified that a ratio $\lambda_2/\lambda_1 < 0.2$ effectively degrades the shift estimation task, and this metric could be used to discard badly conditioned situations.

To compute this ratio, since $\tau = \mathbf{A}^T \mathbf{A}$ is positive definite and symmetric, then both of its eigenvalues λ_1 and λ_2 are real and non-negative and its computation is straightforward.



(a) (b) (c) (d) (e) (f)
 0.021, 0.041 0.057, 0.042 0.115, 0.343 0.063, 0.491 0.004, 0.437 0.002, 0.616
 Figure 7: CRLB and eigenratios respectively for six examples of landscapes. Green represents valid and red implies failure.

5 Results

5.1 Scene pre-selection evaluation

Figures 7a and 7b display two examples of SH landscapes that do not validate the eigenratio test. In these images there is a strong dominant gradient direction that complicates the shift estimation. The aperture problem is visually obvious in both cases. Figures 7c and 7d present a high CRLB. The first one corresponds to a project where the images are composed by only noise, while the second example has a higher SNR, however the noise is still considerable. Finally, two examples of valid landscapes are shown in figures 7e and 7f which were validated by both proposed tests.

5.2 Comparison with state-of-the-art methods

5.2.1 The CNES simulated database

CNES (French space agency) provided realistic simulations of several SHWFS landscapes obtained from earth-observing satellites with their corresponding ground truth. The provided images were 37×37 pixels from a 12×12 grid following the occlusion schema of Fig. 2a. The simulated wavefront aberrations translated into displacements no larger than half a pixel. For each provided landscape, three different SNR settings were simulated. Fig. 8 displays some example landscapes.

Every described state-of-the-art algorithm and our proposed method using different interpolation/gradient estimation approaches was tested against the whole dataset. In table 1 the errors in pixels are displayed for the best performing methods. These are the method from Michau *et al.* [21], the SDF method performing 2D quadratic interpolation (SDF-2QI) from Lofdahl [18], the periodic convolution approach from Poyneer [26] and the iterative APC method from Sidick *et al.* [39]. For the proposed GBSE approach, three variants are considered with increasing computational cost. A fourth variant using the Gaussian derivative estimation method was included for comparison purposes.

The errors obtained for figures 8.1 and 8.2 are close to the theoretical limits predicted by their CRLB. On the other side, the error obtained with Fig. 8.3 and its CRLB implies that a strong improvement is possible. Line 4, corresponding to Fig. 8.4, is an example where every method fails to achieve accurate results, possibly due to the noise and the lack of texture, which is revealed by a lower bound considerably higher than for most other cases. Fig. 8.5 shows an example of a landscape where the Poyneer method [26] as well as PCC [39] are clearly improved by the proposed approach. Fig. 8.6 proves that the aperture problem hinders most shift estimation methods, as evidenced by their resulting errors.

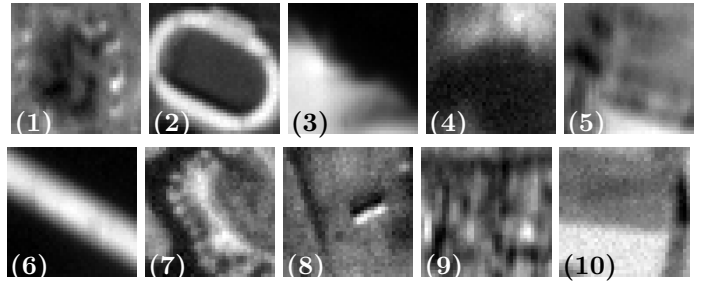


Figure 8: Examples of landscapes from the CNES database.

Table 1: CRLB, EigenRatio (ER) and errors (in pixels) for selected sample landscapes of the CNES database. ^a

	CRLB	ER	[18]	[21]	[26]	[39]	lit	2it L	3it S	lit $\sigma=0.6$
(1)	0.014	0.66	0.019	0.121	0.026	0.054	0.030	0.017	0.016	0.022
(2)	0.006	0.44	0.029	0.106	0.038	0.158	0.014	0.008	0.008	0.013
(3)	0.006	0.19	0.048	0.096	0.105	0.092	0.035	0.036	0.036	0.040
(4)	0.041	0.59	0.127	0.113	0.090	0.794	0.070	0.064	0.069	0.078
(5)	0.011	0.77	0.039	0.113	0.069	0.070	0.026	0.016	0.016	0.022
(6)	0.030	0.01	0.081	0.099	0.083	0.081	0.053	0.043	0.040	0.042
(7)	0.019	0.69	0.023	0.111	0.048	0.134	0.034	0.021	0.021	0.025
(8)	0.026	0.63	0.045	0.114	0.039	0.083	0.048	0.032	0.031	0.037
(9)	0.010	0.34	0.043	0.113	0.029	0.042	0.028	0.015	0.014	0.021
(10)	0.027	0.61	0.065	0.112	0.051	0.645	0.046	0.037	0.043	0.047
Avg.	0.029	132	0.146	0.111	0.491	0.478	0.047	0.039	0.039	0.043
Valid	0.011	64	0.024	0.110	0.048	0.057	0.027	0.018	0.017	0.022
Time			0.296	0.025	0.084	0.221	0.034	0.165	0.311	0.052

^aRows in green represent landscapes considered valid ($CRLB < 0.02$ and $ER > 0.2$), while invalid landscapes are shown in red. Bold indicates lowest error. Averages correspond to the whole dataset, and its ER column displays the amount of landscapes processed. The Valid row represents the averages over all valid landscapes. The first column links each row with the landscapes shown in Fig. 8. Columns [18], [21], [26] and [39] refer to SDF-2QI, Michau *et al.*, Poyneer and APC methods respectively. The variants of our approach lit, 2it L, 3it S represent Alg. 1 using the hypomode derivative with 1, 2 (bilinear interpolation) and 3 (spline interpolation) iterations respectively. The last column stands for one iteration and Gaussian derivative with $\sigma=0.6$

The PCC algorithm particularly failed under the landscape present in Fig. 8.7 although the reason is not evident. Finally, line 9 (Fig. 8.9) shows a case where the SDF-2QI method was outperformed by all variants of the proposed approach.

5.2.2 Simulated experiments

Experimental Setup. We used a simulator to evaluate the performance of the proposed method. Given a 12-bit input image, a set of images was generated matching a SHWFS configuration provided by CNES. A 12×12 lenslet grid occluded as shown in Fig. 2a was assumed. For each lenslet a ground truth shift was randomly generated. Since we were simulating in a closed loop environment, the maximum displacement was kept to half a pixel. Each sub-aperture image was then obtained by DFT resampling the input image, extracting a 37×37 pixels subimage, multiplying by the occlusion factor, and lastly adding noise.

The error for each method was computed as the mean error for all valid sub-apertures. A sub-aperture was considered invalid and therefore discarded if it was occluded on more than 60% of its surface. The error for each sub-aperture was the Euclidean distance between the measured and the ground truth shift. To evaluate the robustness to image content, we used three subimages: a highly contrasted one that should

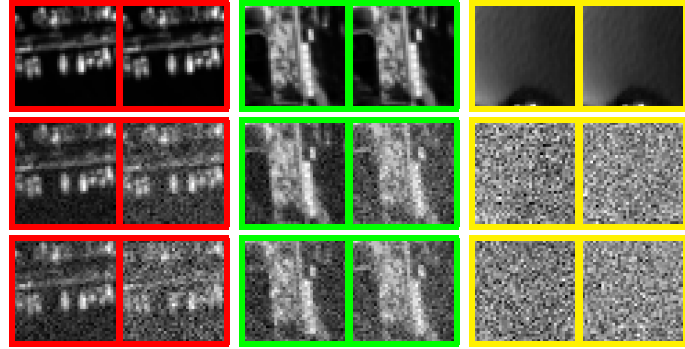


Figure 9: **Top:** Input image used for the simulations. **Bottom:** For each level of noise $\sigma_n = \{1, 100, 200\}$ (vertically separated), two different sub-apertures are shown: no occlusion and 57% occluded (horizontally separated). The dynamic ranges were stretched for viewing purposes.

not present any difficulty for shift estimation, a slightly more challenging one with its gradient mainly distributed on a single direction, and one from the sea with almost no signal (there are just a few pixels of land on the bottom). Different amounts of additive white Gaussian noise were simulated (with standard deviation $\sigma_n \in [1, \dots, 150]$), and all methods were evaluated on 100 noise realizations. Fig. 9 shows the subimages affected by three noise levels. Signal dependent noise was handled by application of a variance stabilization transform. Finally, the processing time of each method was measured using a non-optimized Matlab implementation on an Intel Xeon E5-2650 CPU.

We tested several variants of the proposed GBSE method. Each one was composed by an interpolation method for resampling selected among the five methods proposed (see section 3.3), a gradient estimation method chosen between the hypomode or one of the three Gaussian derivatives with $\sigma_g = \{0.3, 0.6, 1\}$ (section 3.2), and using up to three iterations per shift estimation. Also, different variants using the multiscale approach were evaluated (section 3.5) up to 3 scales, where for each scale, an iterative GBSE algorithm was used with up to 3 iterations. From these methods we retained the best performing non-iterative method ($k = 1$ and no resampling) which uses $\sigma_g = 0.6$ for the gradient computation, and the best one with 3 iterations which uses DFT resampling with image periodization and $\sigma_g = 0.3$. We compared them with all state-of-the-art algorithms presented in section 2. For practical reasons, we only display the best performing ones, namely, the ACC [37] and the APC [39] methods from Sidick presented in section 2.3, and the Poyneer [26] and Löfdahl

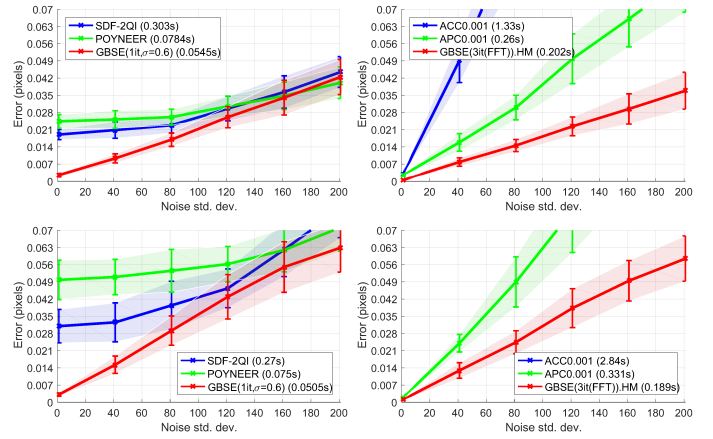


Figure 10: Performance for non-iterative and iterative methods compared to the best variant of the proposed GBSE approach. **Top:** First test image. **Bottom:** Second test image. **Left:** Non-iterative methods. **Right:** Iterative methods.

SDF-2QI algorithm [18] presented in section 2.1. The SDF-2QI algorithm computes the squared sum difference function and searches its maximum by using 2D quadratic interpolation. All other presented methods were also evaluated but discarded due to lower accuracies.

Results in a closed loop system. We compared iterative and non-iterative algorithms separately. The average errors and the standard deviations for non-iterating methods on the first image type are shown in Fig. 10 (top left), together with the processing time. The non-iterative GBSE version using Gaussian derivatives with $\sigma = 0.6$ outperforms both Poyneer and SDF-2QI (which perform similarly in this image). GBSE is also more stable (less variability) and faster. In Fig. 10 (top right) both iterative methods ACC and APC were compared with GBSE using 3 iterations, DFT resampling and the hypomode derivative. Again the proposed method proves to be the most accurate and more stable. Even more, this method is the best also compared to non-iterated methods. Notice the high impact of noise on the ACC method. It is more precise than both non-iterating methods for low ($\sigma \leq 20$). Nevertheless, it diverges for stronger noise. This problem is well-known for phase-correlation methods [26].

The results for the second image type (bottom of Fig. 10) are similar to the first one, although the average errors are higher. While the SDF-2QI performs slightly worse, the Poyneer method is considerably worse. This is due to discrepancies at the image boundaries resulting from the periodicity assumption of the periodic convolution used by Poyneer. This also explains why both ACC and PCC methods behave so poorly on this image. This also implies that computing the shift in the spatial domain is usually more stable than doing so in the frequency domain, unless some windowing is performed, which is prohibitive on such small images where the objects are sometimes close to the image boundaries. Yet again, the proposed methods are more precise, stable and with less variability than the state-of-the-art. The third image type did not pass the verification step and all the methods failed, so its results are omitted.

Results under larger displacements. The same experiment was performed by simulating wavefront aberrations having displacements of up to 4 pixels, to evaluate robustness against high frequency aberrations. In Fig. 11 the average

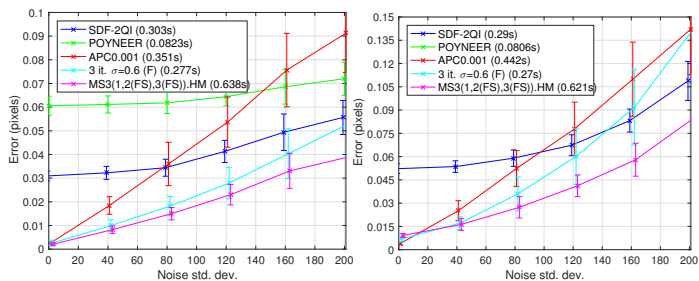


Figure 11: Average error and standard deviations of selected methods and two variants of the proposed GBSE approach when simulating wavefront aberrations yielding displacements of up to 4 pixels. **Left:** First test image. **Right:** Second test image.

error together with the standard deviations are shown for the most representative methods. Due to the larger underlying displacements, multiscale approaches achieve better results as the noise increases, reproducing the results of [29]. In fact, a multiscale approach becomes mandatory if fewer than two iterations are performed, and the best performing method used three scales (where a single iteration was used in the coarsest scale, two iterations with FFTP interpolation in the second scale and three iterations with FFTP interpolation in the final finer scale). Although this method proved to be the most accurate in our tests, it also requires more computational resources as evidenced by its running time. However, using the iterative non-multiscale approach with three iterations and FFT interpolation showed comparable results while requiring fewer processing time. Nevertheless, the method proposed by Poyneer should be considered when lower processing times are required. Indeed, as expected, non-iterated versions of the GBSE algorithm failed when estimating the shift with large underlying displacements. Let us add the caveat that when measuring the aberration using the second slightly challenging landscape (green rectangle in Fig 9), the Poyneer method obtained inaccurate results even under high SNR conditions.

6 Conclusion

A new method for accurate sub-pixel shift-estimation, based on an iterative global optical flow method, was proposed in the context of a SHWFS on extended scenes for on-board aberration correction on earth-observation satellites. Using a telescope simulator developed by CNES, we showed that the proposed algorithm is more accurate, stable, robust to noise, and with lower variability than the current state-of-the-art, permitting a more precise wavefront estimation. By performing on-board real-time mirror correction, this opens the way to cheaper high resolution earth-observation satellites.

It should be noted that although this method was conceived for on-board earth-observation satellites, it could also be used in a ground-based wavefront sensing context. Indeed, for ground-based applications, the demanding processing time requirements existing in satellites are considerably reduced, in which case, due to the availability of more computational resources, the proposed method could still be applicable using more iterations and/or scales. Therefore, it is envisaged to test the proposed algorithm for the case of atmospheric turbulence correction on extended sources.

Funding. Centre National d’Etudes Spatiales (MISS Project); Office of Naval research (grant N00014-14-1-0023); Ministerio de Economía y Competividad, Spain (BES-2012-057113); Agence Nationale de la Recherche (ANR-12-ASTR-0035).

References

- [1] Cecilia Aguerrebere, Mauricio Delbracio, Alberto Bartesaghi, and Guillermo Sapiro. Fundamental limits in multi-image alignment. *CoRR*, abs/1602.01541, 2016.
- [2] F. J. Anscombe. The transformation of poisson, binomial and negative-binomial data. *Biometrika*, 35(3/4):246–254, 1948.
- [3] Simon Baker and Iain Matthews. Lucas-kanade 20 years on: A unifying framework. *IJCV*, 56(3):221–255, 2004.
- [4] G. M. Bernstein and D. Gruen. Resampling Images in Fourier Domain. *Publications of the Astronomical Society of the Pacific*, 126:287–295, March 2014.
- [5] A. Bonnefois et al. Comparative theoretical and experimental study of a Shack-Hartmann and a Phase Diversity Sensor, for high-precision wavefront sensing dedicated to Space Active Optics. In *ICSO 2014*, October 2014.
- [6] Martin J Booth. Adaptive optics in microscopy. *Philosophical Transactions of the Royal Society of London A: Mathematical, Physical and Engineering Sciences*, 365(1861):2829–2843, 2007.
- [7] Peter J Burt and Edward H Adelson. The laplacian pyramid as a compact image code. *Communications, IEEE Transactions on*, 31(4):532–540, 1983.
- [8] Peter C Chen, Charles W Bowers, Marzouk Marzouk, and Robert C Romeo. Advances in very lightweight composite mirror technology. *Optical Engineering*, 39(9):2320–2329, 2000.
- [9] Carl De Boor. *A practical guide to splines; rev. ed.* Applied mathematical sciences. Springer, Berlin, 2001.
- [10] M. Elad, P. Teo, and Y. Hel-Or. Optimal filters for gradient-based motion estimation. In *Computer Vision, 1999. The Proc. of the Seventh IEEE Int. Conf. on*, volume 1, pages 559–565 vol.1, 1999.
- [11] C. Escolle, E. Hugot, T. Fusco, M. Ferrari, V. Michau, and T. Bret-Dibat. Adapting large lightweight primary mirror to space active optics capabilities. (JUNE):915128, 2014.
- [12] H. Foroosh, J.B. Zerubia, and M. Berthod. Extension of phase correlation to subpixel registration. *Image Processing, IEEE Transactions on*, 11(3):188–200, mar 2002.
- [13] Dennis C Ghiglia and Mark D Pritt. *Two-dimensional phase unwrapping: theory, algorithms, and software*, volume 4. Wiley New York, 1998.

- [14] D Gratadour, LM Mugnier, and D Rouan. Sub-pixel image registration with a maximum likelihood estimator. *Astronomy & Astrophysics*, 443(1):357–365, 2005.
- [15] Jan Herrmann. Least-squares wave front errors of minimum norm. *JOSA*, 70(1):28–35, 1980.
- [16] R. Keys. Cubic convolution interpolation for digital image processing. *IEEE Transactions on Acoustics, Speech, and Signal Processing*, 29(6):1153–1160, Dec 1981.
- [17] Per Knutsson, Mette Owner-Petersen, and Chris Dainty. Extended object wavefront sensing based on the correlation spectrum phase. *Optics express*, 13(23):9527–9536, 2005.
- [18] Mats G Löfdahl. Evaluation of image-shift measurement algorithms for solar shack-hartmann wavefront sensors. *Astronomy & Astrophysics*, 524:A90, 2010.
- [19] Bruce D. Lucas and Takeo Kanade. An iterative image registration technique with an application to stereo vision. *IJCAI'81*, pages 674–679. Morgan Kaufmann Publishers Inc., 1981.
- [20] V Michau, J-M Conan, T Fusco, M Nicolle, C Robert, M-T Velluet, and E Piganeau. Shack-hartmann wavefront sensing with extended sources. In *SPIE Optics+Photonics*, pages 63030B–63030B. SPIE, 2006.
- [21] V Michau, G Rousset, and J Fontanella. Wavefront sensing from extended sources. In *Real Time and Post Facto Solar Image Correction*, volume 1, page 124, 1993.
- [22] Rhonda M Morgan, Kirill V Shcheglov, Joseph J Green, Catherine M Ohara, Jennifer Roberts, and Erkin Sidick. Testbed for extended-scene shack-hartmann and phase retrieval wavefront sensing. In *Optics & Photonics 2005*, pages 59030I–59030I. International Society for Optics and Photonics, 2005.
- [23] T. Q. Pham, M. Bezuijen, L. J. Van Vliet, K. Schutte, and C. L. L. Hendriks. Performance of optimal registration estimators. In *Proc. SPIE*, volume 5817, pages 133–144, 2005.
- [24] T.Q. Pham and M. Duggan. Bidirectional bias correction for gradient-based shift estimation. In *Image Processing, 2008. ICIIP 2008. 15th IEEE International Conf. on*, pages 829–832, Oct 2008.
- [25] Ben C Platt et al. History and principles of shack-hartmann wavefront sensing. *Journal of Refractive Surgery*, 17(5):S573–S577, 2001.
- [26] Lisa A Poyneer. Scene-based shack-hartmann wavefront sensing: analysis and simulation. *Applied Optics*, 42(29):5807–5815, 2003.
- [27] Lisa A. Poyneer, Donald T. Gavel, and James M. Brase. Fast wave-front reconstruction in large adaptive optics systems with use of the fourier transform. *J. Opt. Soc. Am. A*, 19(10):2100–2111, Oct 2002.
- [28] Lisa A. Poyneer, David W. Palmer, Kai N. LaFortune, and Brian Bauman. Experimental results for correlation-based wavefront sensing. In Mark T. Gruneisen, John D. Gonglewski, and Michael K. Giles, editors, *Optics & Photonics 2005*, pages 58940N–58940N–142. International Society for Optics and Photonics, August 2005.
- [29] Martin Rais, J.-M. Morel, and Gabriele Facciolo. Iterative gradient-based shift estimation: To multiscale or not to multiscale? In *Progress in Pattern Recognition, Image Analysis, Computer Vision, and Applications - 20th Iberoamerican Congress, CIARP 2015, Montevideo, Uruguay, November 9-12, 2015, Proceedings*, pages 416–423, 2015.
- [30] Clélia Robert, Jean-Marc Conan, Vincent Michau, Thierry Fusco, and Nicolas Vedrenne. Scintillation and phase anisoplanatism in shack-hartmann wavefront sensing. *JOSA A*, 23(3):613–624, 2006.
- [31] D. Robinson and P. Milanfar. Fundamental performance limits in image registration. *Image Processing, IEEE Transactions on*, 13(9):1185–1199, Sept 2004.
- [32] Dirk Robinson and Peyman Milanfar. Bias minimizing filter design for gradient-based image registration. *Signal Processing: Image Communication*, 20(6):554 – 568, 2005. Special Issue on Advanced Aspects of Motion Estimation Special Issue on Advanced Aspects of Motion Estimation.
- [33] M. Roopashree, A. Vyas, and B Raghavendra Prasad. Performance analysis of Fourier and Vector Matrix Multiply methods for phase reconstruction from slope measurements. *ArXiv e-prints*, November 2009.
- [34] B. Rouge, H. Vadon, and A. Giros. Fine stereoscopic image matching and dedicated instrument having a low stereoscopic coefficient, November 22 2011. US Patent 8,064,687.
- [35] Gerard Rousset. Wave-front sensors. *Adaptive optics in astronomy*, 1:91, 1999.
- [36] Shinsuke Shimojo, Gerald H. Silverman, and Ken Nakayama. Occlusion and the solution to the aperture problem for motion. *Vision Research*, 29(5):619 – 626, 1989.
- [37] E. Sidick et al. An Adaptive cross-correlation algorithm for extended scene Shack-Hartmann wavefront sensing. In *Adaptive Optics: Methods, Analysis and Applications*. OSA, 2007.
- [38] E. Sidick, R. Morgan, J. Green, C. Ohara, and D. Redding. Adaptive Cross-Correlation Algorithm and Experiment of Extended Scene Shack-Hartmann Wavefront Sensing. In Howard A. MacEwen and James B. Breckinridge, editors, *UV/Optical/IR Space Telescopes: Innovative Technologies and Concepts III*, volume 6687, pages 668710–668711, September 2007.
- [39] Erkin Sidick. Adaptive periodic-correlation algorithm for extended scene shack-hartmann wavefront sensing. In *Imaging and Applied Optics*, page CPDP1. Optical Society of America, 2011.

- [40] E.P. Simoncelli. Design of multi-dimensional derivative filters. In *Image Processing, 1994. Proc. ICIP-94., IEEE Int. Conf.*, volume 1, pages 790–794 vol.1, Nov 1994.
- [41] William H Southwell. Wave-front estimation from wave-front slope measurements. *JOSA*, 70(8):998–1006, 1980.
- [42] H.S. Stone, M.T. Orchard, E.-C. Chang, and S.A. Marucci. A fast direct fourier-based algorithm for subpixel registration of images. *Geoscience and Remote Sensing, IEEE Transactions on*, 39(10):2235–2243, Oct 2001.
- [43] T. Tarbell and R. Smithson. A Simple Image Motion Compensation System for Solar Observations. *Solar instrumentation: What's next? Proc. of a Conf.*, 1981.
- [44] Robert Tyson. *Principles of adaptive optics*. CRC press, 2010.
- [45] Robert K Tyson. Bit-error rate for free-space adaptive optics laser communications. *JOSA A*, 19(4):753–758, 2002.
- [46] Nicolas Védrenne, Vincent Michau, Clélia Robert, and Jean-Marc Conan. Shack-Hartmann wavefront estimation with extended sources: anisoplanatism influence. *Journal of the Optical Society of America A*, 24(9):2980, September 2007.
- [47] A. Wirth. Ophthalmic instrument having hartmann wavefront sensor with extended source, July 22 2003. US Patent 6,595,642.
- [48] P Wizinowich et al. First light adaptive optics images from the Keck II telescope: a new era of high angular resolution imagery. *Publications of the Astronomical Society of the Pacific*, 112(769), 2000.